

Supplementary Information

for

Cilostazol-imprinted polymer film-coated electrode as an electrochemical chemosensor for selective determination of cilostazol and its active primary metabolite

*Jyoti,^a Renata Rybakiewicz-Sekita,^{b,c} Teresa Żolek,^d Dorota Maciejewska,^d Edyta Gilant,^e
Katarzyna Buś-Kwaśnik,^e Andrzej Kutner,^f Krzysztof R. Noworyta,^{a,*} and
Włodzimierz Kutner^{a,b,*}*

^a Institute of Physical Chemistry, Polish Academy of Sciences, Kasprzaka 44/52, 01-224 Warsaw, Poland

^b Faculty of Mathematics and Natural Sciences. School of Sciences, Institute of Chemical Sciences, Cardinal Stefan Wyszyński University in Warsaw, Wóycickiego 1/3, 01-815 Warsaw, Poland

^c Laboratory of Organic Electronics, Linköping University, Bredgatan 33, 602 21 Norrköping, Sweden

^d Department of Organic Chemistry, Faculty of Pharmacy, Medical University of Warsaw, Banacha 1, 02-097, Warsaw, Poland

^e Łukasiewicz Research Network – Industrial Chemistry Institute, Rydygiera 8, 01-793, Warsaw, Poland

^f Department of Bioanalysis and Drug Analysis, Faculty of Pharmacy, Medical University of Warsaw, Banacha 1, 02-097 Warsaw, Poland

E-mail addresses: knoworyta@ichf.edu.pl (K. Noworyta) and wkutner@ichf.edu.pl (W. Kutner).

S1. Instrumentation, techniques, and procedures

An SP-300 potentiostat/galvanostat computerized electrochemical system of Bio-Logic, SAS, controlled by EC-Lab V10.37 software of the same manufacturer, was used for electrochemical measurements. In these measurements, a three-electrode one-compartment V-shaped glass electrochemical minicell was used. A 0.75-mm diameter Pt disk, sealed in a soft glass tubing, and Ag and Pt wires served as the working, quasi-reference, and counter electrode, respectively. The minicell and electrodes were designed and fabricated in the IPC PAS mechanical workshop.

The surface of MIP-CIL and control non-imprinted polymer (NIP) was imaged with scanning electron microscopy (SEM) using a Nova NanoSEM 450 microscope of the FEI Nova and atomic force microscopy (AFM) using a MultiMode 8 AFM microscope under the control of a Nanoscope V controller and Multimode v 8.15 software, both from Bruker. An antimony-doped Si tip and cantilevers of 376-kHz resonant frequency and the force constant, $k = 60$ N/m, were used for the Tapping Mode™ sample imaging. The MIP and NIP films were deposited on Au film-coated, with Ti underlayer, (7 × 25) mm² glass slides using a homemade holder with the Pt plate counter electrode and the Ag wire quasi-reference electrode. For roughness measurements, four points of the sample were imaged at (5 × 5) μm². Then average roughness was calculated from the results obtained for each image. Roughness calculations of a single image were performed by using NanoScope Analysis v. 1.2 software from Bruker.

Polarization-modulation infrared reflection-absorption spectroscopy (PM-IRRAS) spectra for the MIP and NIP films were recorded with a Vertex 80v spectrophotometer equipped with PMA 50 module and controlled with OPUS v 7.2 software (Bruker) under ambient atmosphere using a liquid-nitrogen cooled B316/6 MCT detector. For each spectrum, 1024 scans with a spectral resolution of 2 cm⁻¹ were acquired and then averaged.

S2. Electrochemical measurements

All CV and DPV measurements were performed at room temperature, 20 (±1) °C, using the electrochemical mini cell and 10-mM ferrocene redox probe in 0.1 M (TBA)ClO₄, in DCM. In the DPV measurements, the potential was scanned from 0 to 0.70 V vs. Ag/AgCl with the potential step of 5 mV. The amplitude of 50-ms pulses applied was 25 mV. Single images were performed by using NanoScope Analysis v. 1.2 software from Bruker.

S3. Synthesizing monomers

Syntheses of the 4-[3,6-di(thiophen-2-yl)-9H-carbazol-9-yl]benzoic acid (FM1), Figure 1a, and 1,4-bis(3,6-di(thiophen-2-yl)-9H-carbazol-9-yl)benzene (CLM), Figure 1b, are described elsewhere.¹

S4. Synthesizing and depositing the MIP and NIP films

The MIP was synthesized and simultaneously deposited as a thin film on the electrode surface under potentiodynamic conditions (Figure 3a). A DCM solution of 0.1 mM CIL template, 0.3 mM FM1 functional monomer, 0.3 mM CLM cross-linking monomer, and 0.1 M (TBA)ClO₄ supporting electrolyte was used for this electropolymerization. Two potential cycles between 0 and 1.0 V vs. Ag quasi-reference electrode were performed at a 100-mV s⁻¹ scan rate (Figure 3). After that, the electrode was twice rinsed with DCM. Finally, CIL was extracted from the MIP film with 10 mM NaOH for 30 min. The NIP films were deposited without the CIL template (Figure 3b) and treated similarly to the MIP films. Polymer films were deposited on Pt disk electrodes of 0.75 mm in diameter or Au film-layered glass slides. Before electropolymerization, Pt electrodes were cleaned with the "Piranha" solution. (Warning. This solution is dangerous if contacting skin or eye.) Then, the surfaces of these electrodes were matted by wiping them with sandpaper of the grain size of 1000. The Au film-coated glass slides were first cleaned with the "Piranha" solution, then rinsed with water, next with 2-propanol, and finally dried before use.

S5. Preparing CIL or dhCIL spiked plasma solutions

Stock solutions of 1.0 mg/mL CIL and 0.1 mg/mL dhCIL were prepared by dissolving weighed portions of the CIL and dhCIL reference standards in methanol. Working solutions were prepared by diluting stock solutions with a mixed solution of methanol: 0.1% formic acid (1 : 1, v/v). Human plasma samples donated by healthy volunteers (with the citrate anticoagulant added) were prepared by adding the blank plasma with the appropriate working solution at a volume ratio of 12.5 : 1. The CIL concentration ranged from 27.1 to 8120 nM in CIL spiked human plasma samples, whereas the dhCIL concentration in these samples was 81.6 nM (Table 2). The samples were split into two parts for simultaneous CIL and dhCIL determining with the MIP-film electrochemical chemosensing and LC-MS.

S6. Cilostazol (CIL) and 3,4-dehydrocilostazol (dhCIL) determining in spiked human plasma using LC-MS

In spiked human plasma, CIL and dhCIL were determined using LC-MS. The liquid-liquid extraction with a mixed solvent solution of 1-butanol : chloroform : tert-butyl methyl ether (3 : 20 : 77, v/v/v) was used for sample preparation. The sample components were separated using LC-MS on the Zorbax SB-C18 150 × 3.0 mm, 3.5 μm column (Agilent Technologies, USA) at 50 (±2) °C. A mixed solvent solution of 0.01% formic acid, methanol, and acetonitrile (50: 25: 25, v/v/v) served as the mobile phase. Positive electrospray ionization mass spectrometry in single-ion monitoring mode was applied to determine CIL and dhCIL. Isotope-labeled CIL (cilostazol-d11) was used as the internal standard. CIL ions, the internal standard, and dhCIL were monitored at the respective m/z ratio of 370.1, 381.1, and 368.0. The total analysis run time was 10 min. The method was validated, and the study was performed in compliance with the OECD Principles of Good Laboratory Practice (GLP).

S7. Cilostazol (CIL) and 3,4-dehydrocilostazol (dhCIL) determining in spiked human plasma using MIP chemosensor

The plasma samples spiked with known CIL concentration, determined with LC-MS, were thawed in air and then diluted with DCM. Next, the resulting mixture was vortexed (3000 rpm) for a few minutes and then left to separate the organic and aqueous phases. Afterward, the organic phase was collected and then centrifuged for 10 min at 10,000 g to separate the slug. The supernatant samples, 3518.6 and 8120 nM in CIL (Samples No. 4 and 5 in Table 2), were diluted 10 times. However, samples 27.1, 81.2, and 676.7 nM in CIL and 81.6 nM in dhCIL were not diluted at all. To each sample, (TBA)ClO₄ and ferrocene were added to reach the 0.1 M and 10 mM concentrations, respectively. A 1-mL sample of the above ferrocene redox probe solution was placed in an electrochemical mini cell. The MIP-CIL film-coated electrode was immersed in this solution, and the DPV current was measured. The resulting changes in the DPV peak currents were then used for constructing calibration plots and calculating recovery.

S8. Computer simulations of model structures of pre-polymerization complexes and imprinted cavities complexes with analytes and interferences

All-atom molecular dynamic (MD) simulations were performed with the Discovery Studio 2017R2 with a visual interface BIOVIA² on a PC class machine equipped with 2 Intel Xeon Processors and 32 GB of RAM working under Windows (Microsoft) operating system. The starting molecular structures of CIL, dhCIL, cholesterol, dehydroaripiprazole, FM1, as well as FM2 and FM3 (Scheme S1), and CLM used in simulations of all systems were constructed based on crystallographic atom coordinates³ or the analogy to similar compounds. Their structures in DCM were optimized using density functional theory (DFT) with a B3LYP/6-311G(d,p) hybrid functional implemented in the Gaussian 16 program.⁴ The so-called electrostatic potential (ESP) atomic partial charges on the atoms were computed using the Breneman model,⁵ reproducing the molecular electrostatic potential (MEP). After constructing model systems, preliminary energy minimizations with the 5000 steepest descents and 5000 conjugate gradient steps were carried out. Those were performed to remove irrelevant van der Waals (vdW) contacts using molecular mechanics (MM) with a CHARMM force field.⁶ The processes were applied until the root-mean-square gradient of the structure fell below 4.18×10^{-2} kJ/mol Å. The final MD protocol involved stepped heating from 0 to 294 K for 100 ps at constant volume before an isothermal equilibration step at constant pressure (294 K and 1 bar, respectively) to ensure that the system evolved to achieve a stable density and energy. The statistical data were extracted from these equilibrated NPT (N – amount of substance, P – pressure, and T – temperature) systems during a 5-ns production phase under NVT (N – amount of substance, V – volume, and T – temperature) conditions. In these simulations, periodic boundary conditions were employed together with a 10-Å nonbonded interaction cut-off treating long-range electrostatic interactions with the particle mesh Ewald (PME) simulation method.^{7,8} All bonds to hydrogen atoms were constrained using the SHAKE algorithm, allowing the set time step. The energies and the structures used in all analyzes were from the trajectory file data generated from the last 2 ns MD simulation. The solvation effect was considered explicitly by adding 550 DCM molecules to all constructed systems using the PACKMOL software,⁹ considering that the polymerization and sorption proceeded in DCM. The pre-polymerization complexes (PPCs) and cavities in MIPs were built in subsequent steps. The starting PPCs' structures were composed with the CIL template molecule surrounded by six appropriate FM1, FM2, or FM3 functional monomer molecules. Then, molecules were chosen with MD by considering the strongest interactions with CIL and the molar ratio of the synthetic procedure, namely, 1 : 3. Next, the obtained complex structures were optimized again at the MD

level. An auxiliary potential restraining was applied to the bithiophene-carbazole molecules for retaining the defined structures. A harmonic distance restraint (force constant of 83.74 kJ mol⁻¹ Å²) was sufficient for the calculations. Afterward, six CLM molecules were added to the pre-polymerization complex systems at random positions. After subsequent MD optimization, three CLM molecules were left, reflecting the complex stoichiometry of CIL : FM : CIL (1 : 3 : 3) adopted in the synthetic procedure. After all the optimizations, the PPCs' structures were defined, and the Gibbs free energy change ΔG_C , associated with the formation of different system components were calculated according to Equation 1.

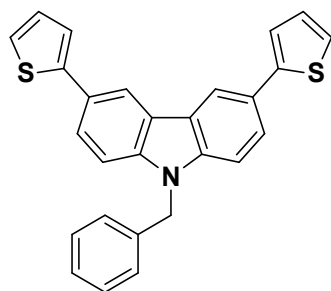
$$\Delta G_C = \Delta G_{complex} - \Delta G_{template} - 3 \times \Delta G_{functional\ monomer} - 3 \times \Delta G_{cross-linking\ monomer} \quad (1)$$

In this equation, $\Delta G_{complex}$ refers to PPC formation, $\Delta G_{template}$ is the separate template formation energy change, $\Delta G_{functional\ monomer}$ is the separate functional monomer formation energy change, $\Delta G_{cross-linking\ monomer}$ is the separate cross-linking monomer formation energy change, and ΔG_C characterizes the PPC stability.

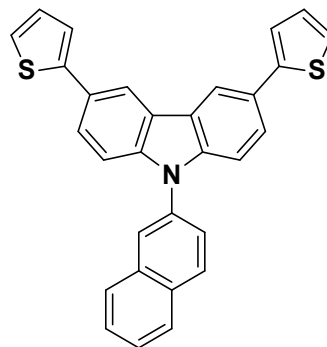
The imprinted molecular cavity was constructed for a selected PPC by simulating the electropolymerization. It was assumed that molecules mainly formed covalent bonds in mutual close vicinity.⁸ Therefore, C2 atoms of thiophene moieties in neighboring molecules of FM1 and CLM were connected with covalent bonds. The resulting structure was optimized, and, after template removal, free space left was proposed as the imprinted cavity. In the final stage, the polymer capacity of analyte sorption was analyzed. CIL and its dhCIL metabolite and the cholesterol and dehydroaripiprazole interferences were considered. For that purpose, the CIL molecule was inserted in the molecular cavity again, and MD was used to simulate its interaction with the cavity in DCM. The same procedure was executed for molecules of dhCIL, cholesterol, and dehydroaripiprazole. The constraints were set on heavy atoms forming polymer matrix with a force constant of 418.68 kJ mol⁻¹ Å² to immobilize the 3-D structure of the cavity during MD calculations. All molecules were left freely, mimicking the sorption step. The changes in Gibbs free energy (ΔG_{bind}) due to the sorption of CIL, dhCIL, and the interferences were calculated using Equation 2.

$$\Delta G_{bind} = \Delta G_{system} - \Delta G_{cavity} - \Delta G_{analyte/interference} \quad (2)$$

In this equation, the Gibbs free energy change of ΔG_{system} is attributed to imprinted cavity sorption of dhCIL, cholesterol, and dehydroaripiprazole. The ΔG_{cavity} accompanies cavity formation, and $\Delta G_{\text{analyte/interference}}$ is due to the formation of the template, its metabolite, or interference molecules.



FM2



FM3

Scheme S1. Structural formulas of the 9-benzyl-3,6-di(thiophen-2-yl)-9H-carbazole (FM2) and 9-(naphthalen-2-yl)-3,6-di(thiophen-2-yl)-9H-carbazole (FM3) functional monomers used to simulate interactions with CIL in DCM using DFT with the B3LYP basis set at the 3-21G(d) level, at room temperature.

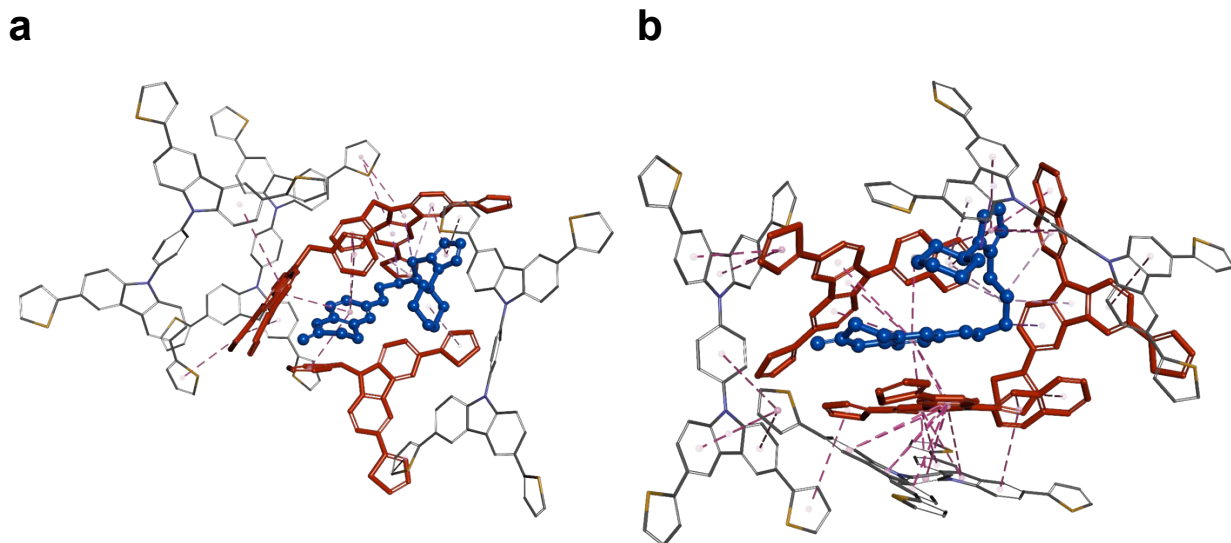


Figure S1. Simulated structures of the pre-polymerization complexes of (a) cilostazol (CIL) with 9-benzyl-3,6-di(thiophen-2-yl)-9H-carbazole (FM2), PPC2, and (b) 9-(naphthalen-2-yl)-3,6-di(thiophen-2-yl)-9H-carbazole (FM3), PPC3. The 1,4-bis(3,6-di(thiophen-2-yl)-9Hcarbazolo-9-yl)benzene cross-linking monomer (CLM) is present in all structures.

S9. Selecting functional monomers

The most promising monomer has the carboxyl on its benzene ring, and its intermolecular interactions seem crucial in the pre-polymerization complex PPC1 formation. The carboxyl is engaged in the strong H-bond (length of 2.47 Å) with the tetrazole ring of CIL and also in the formation of three non-classical hydrogen bonds (π -donor) with the benzene rings of two CLM molecules (length of 2.75 to 3.22 Å). The aromatic conjugated system in all PPC1 components allows for many hydrophobic contacts as π - π T-shaped, π -alkyl, and π - π stacked types. These interactions are between the tetrazole, the butoxy, or the cyclohexyl moieties of CIL and the benzene ring of FM1 or CLM (length of 4.67 to 5.48 Å) as well as between the quinolinone part of CIL and the aromatic rings of FM1 (length of 4.05 to 5.35 Å). Both PPC2 and PPC3 complexes (formed with monomers without the carboxyl, i.e., bearing only aromatic rings) do not form any hydrogen bonds (Figure S1 in Supplementary Information). The hydrophobic interactions (π - π T-shaped, π -alkyl, and π -sigma type) generated are described below. In PPC2, CIL establishes hydrophobic contacts through the quinolinone moiety with the benzyl moiety of three molecules of FM2 (length of 5.16 to 5.33 Å). Between the tetrazole ring or the butoxy linker of CIL and the tricyclic carbazole structure of FM2 (length of 2.70 to 4.94 Å), and between the CIL cyclohexyl

ring and the FM2 thiophene ring of additional hydrophobic interactions are formed. Besides, FM2 molecules create numerous interactions with the CLM molecules, presumably stabilizing the pre-polymerization complex, but these are not specific.

In PPC3, the π - π T-shaped, π -alkyl, π - π stacked and π -sigma type interactions are generated between the tetrazole, the butoxy or the quinolinone moieties of CIL, and the naphthalene or the tricyclic carbazole moieties of FM3 (length of 4.75 to 5.42 Å). As in PPC2, CIL also interacts with only one molecule of CLM. That is, there is one π - π T-shaped interaction between the CIL tetrazole ring and the CLM benzene ring). Moreover, strong hydrophobic interactions (length of 3.66 to 5.67 Å) between FM3 molecules are formed. They can weaken the FM3 interactions with CIL. Considering the above theoretical and experimental results, we proposed PPC1 as the most appropriate candidate for synthesizing the MIP film.

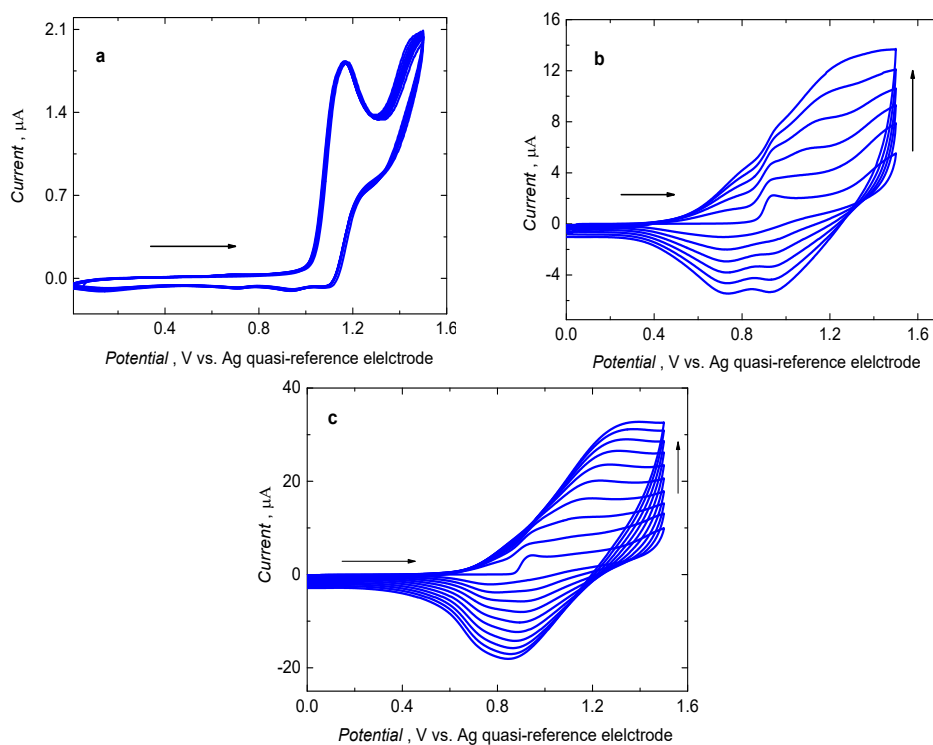


Figure S2. Multi-cyclic potentiodynamic curves for (a) CIL, (b) FM1, and (c) CLM at a 0.75-mm diameter Pt disk electrode at a 100-mV s^{-1} scan rate.

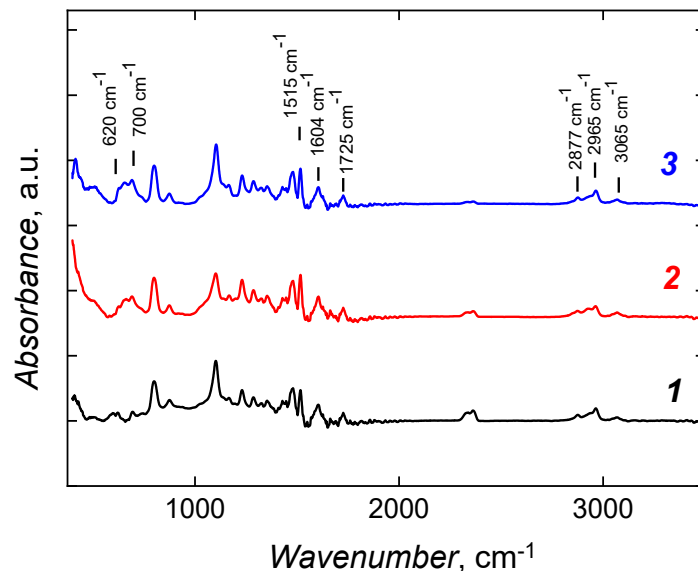


Figure S3. PM-IRRAS spectra for MIP film-coated electrodes (1) before and (2) after 30-min CIL extraction with 10 mM NaOH, and (3) the NIP film-coated electrode.

S10. Characterizing deposited MIP and NIP films

Weak bands at ~ 3065 , ~ 2965 cm^{-1} , and 2877 cm^{-1} in the spectra of all deposited films may be assigned to C-H bond stretching vibration in aromatic and aliphatic moieties, respectively. Moreover, a well-pronounced band at 1725 cm^{-1} was present in the spectra of all films. It originated from C=O bond stretching, thus confirming successful copolymerization and deposition of all monomers present in the pre-polymerization complex solution. This inference is supported by the presence of the 1515 cm^{-1} band corresponding to C-C aromatic ring stretching and a 1604 cm^{-1} band characteristic for C-C stretching of the carbazole moiety. However, a low-intensity band in the $620 - 700$ cm^{-1} region was not evident in the MIP film's spectrum before extraction. The MIP film was relatively thin, and therefore, its CIL content was low compared to the monomers' contents. Therefore, presumably, this band is suppressed when CIL interacts with the polymer film. However, this band appeared in both the MIP and NIP film spectrum after CIL extraction. That confirms the template CIL presence in the deposited MIP film and then its successful removal by extraction. The AFM imaging contributed to a deeper characterization of the MIP and NIP films (Table S1 in Supplementary Information).

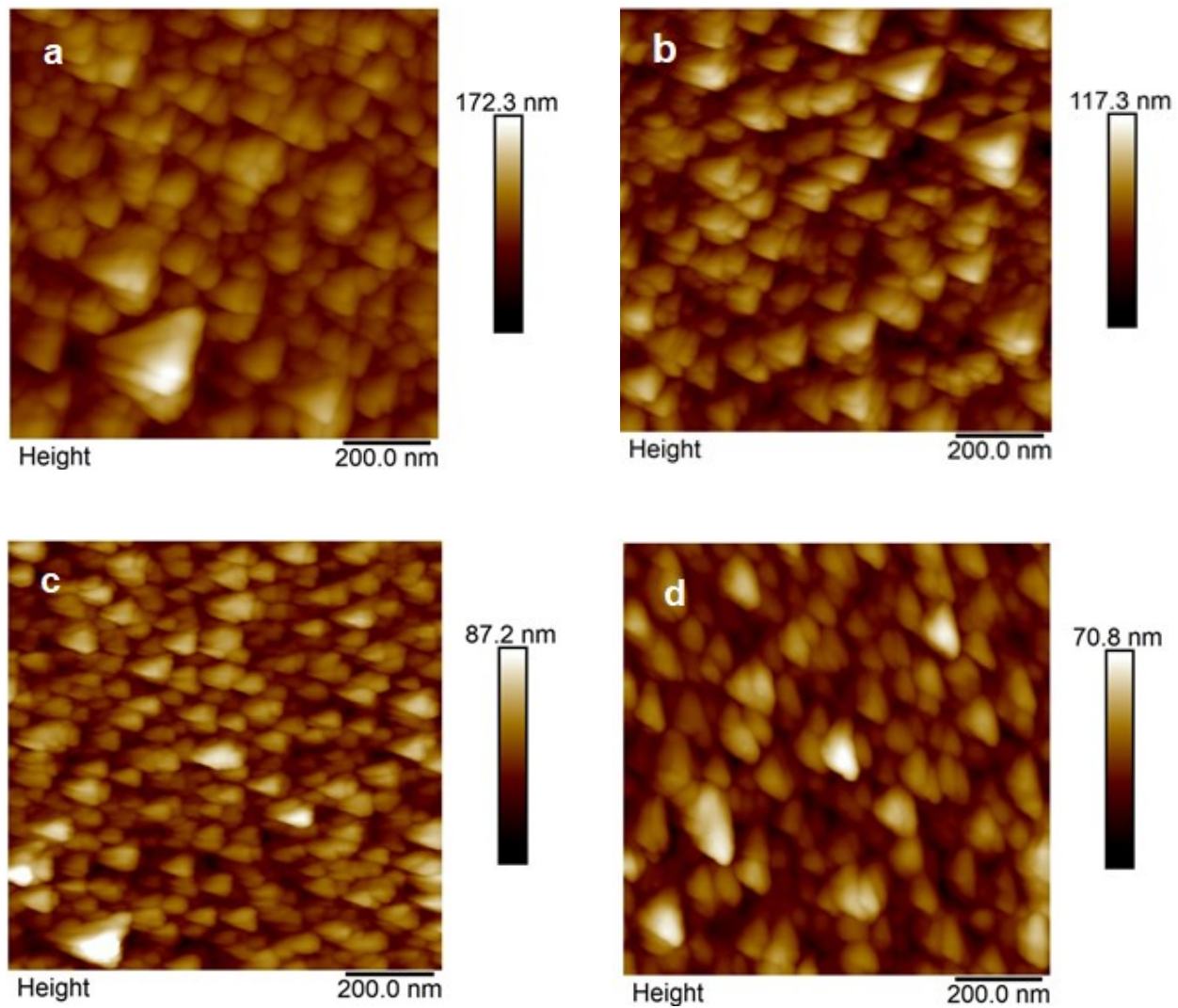


Figure S4. AFM images of (a, b) MIP and (c, d) NIP film-coated (glass slide)/Ti/Au electrodes (a, c) before and (b, d) after 30-min CIL extraction with 10 mM NaOH.

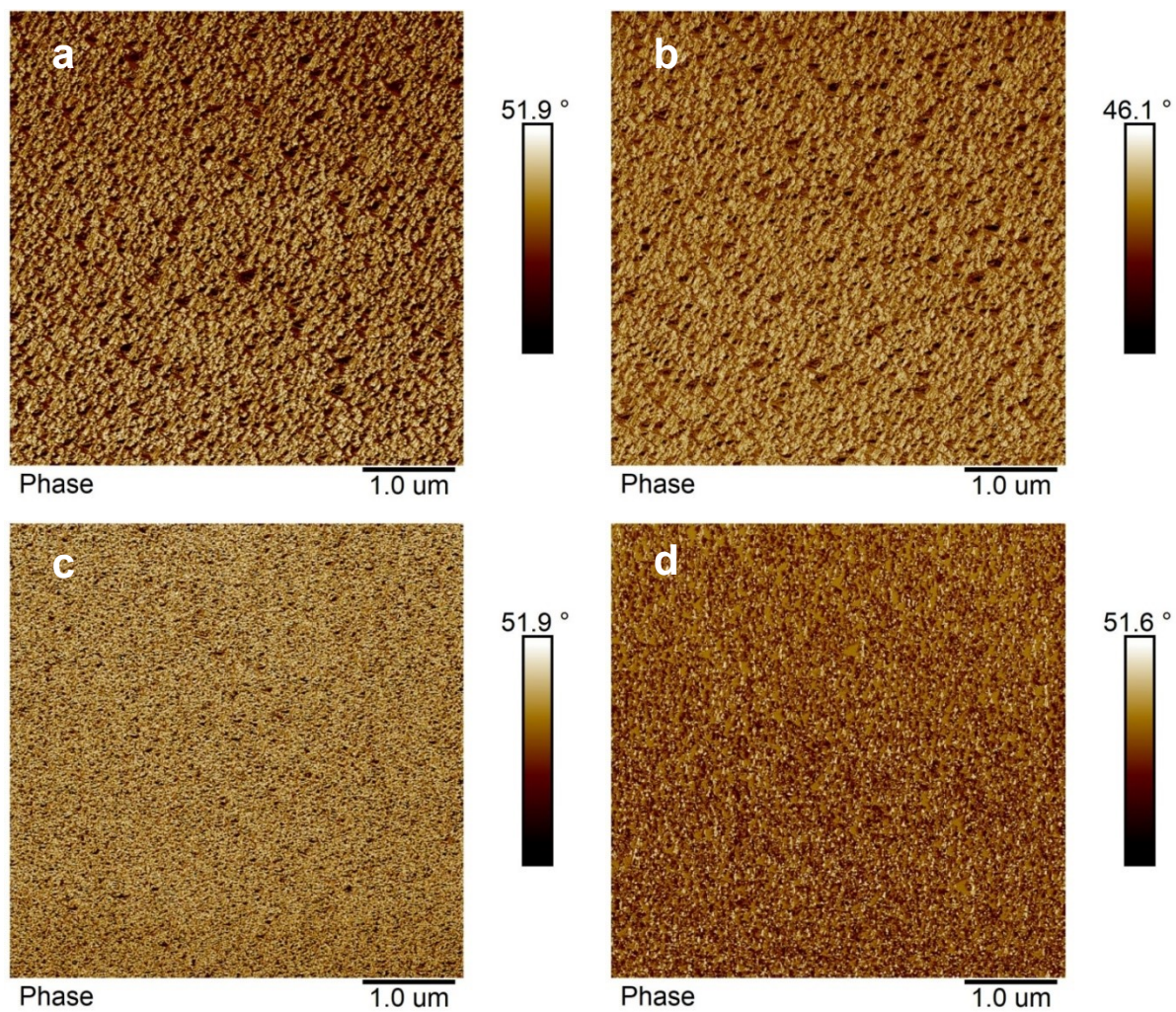


Figure S5. AFM phase images of (a, b) MIP and (c, d) NIP film-coated (glass slide)/Ti/Au electrodes (a, c) before and (b, d) after 30-min CIL extraction with 10 mM NaOH.

Table S1. The MIP and NIP film morphological and nanomechanical parameters derived from the AFM images in Figures S4 and S5 of Supplementary Information.

Polymer film	Film thickness, nm	Film roughness R_a, nm	Phase, degree	Force, nN
MIP-CIL as deposited	96 ± 2	12.7 ± 0.3	15.4 ± 0.1	0.942 ± 0.001
NIP as deposited	44 ± 6	9.5 ± 0.1	20.0 ± 0.2	0.999 ± 0.001
CIL-extracted MIP	69 ± 5	13.8 ± 1.0	24.8 ± 0.1	0.988 ± 0.001
NIP after CIL extraction	57 ± 1	7.6 ± 0.2	1.8 ± 0.8	1.000 ± 0.001

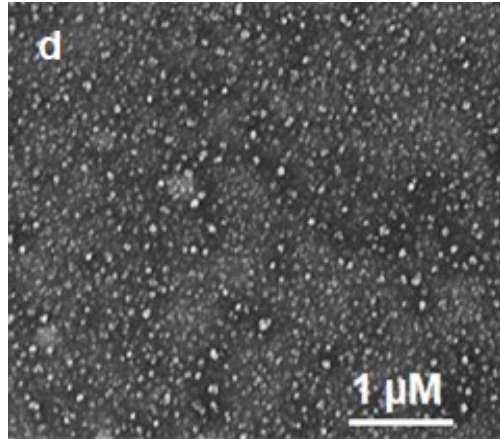
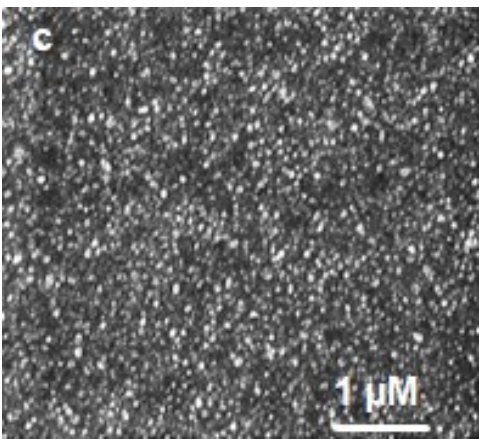
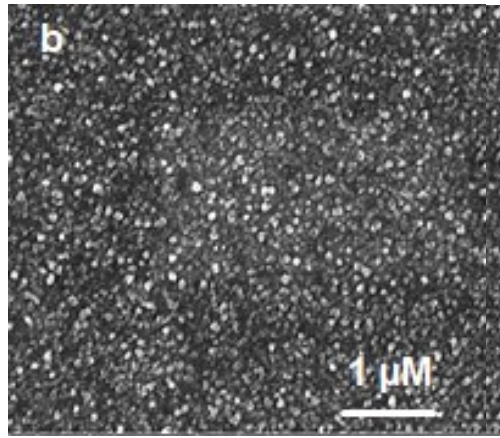
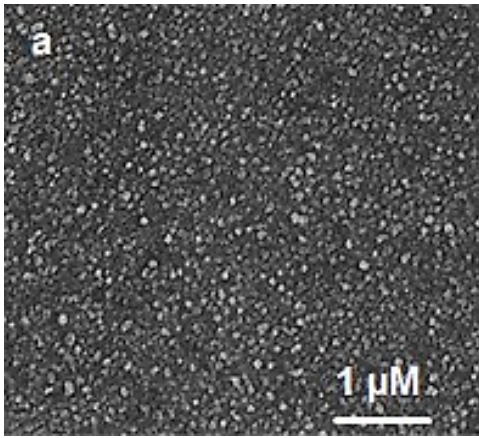


Figure S6. SEM images of the (a, b) MIP and (c, d) NIP film-coated (glass slides)/Ti/Au electrodes (a, c) before and (b, d) after 30-min CIL extraction with 10 mM NaOH.

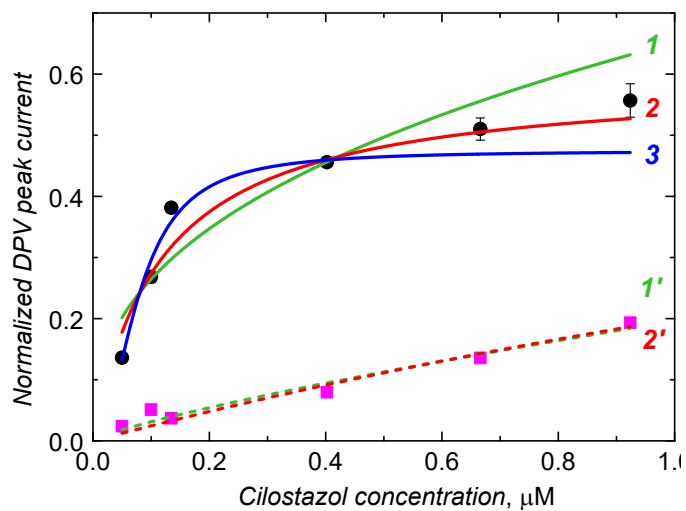


Figure S7. The normalized DPV peak current change with the CIL concentration change for 0.75-mm diameter Pt disk electrodes coated with the film of (1, 2, and 3) CIL-extracted MIP (solid curves) and (1', and 2') NIP (dash curves) in 10 mM ferrocene and 0.1 M (TBA)ClO₄ in DCM. The data points were fitted with the (1) and (1') Freundlich (green), (2) and 2') Langmuir (red), and (3) Langmuir-Freundlich (blue) isotherms.

Table S2a. Parameters of isotherms fitted to the normalized DPV peak current dependence on the CIL concentration at the MIP film-coated electrode depicted in Figure S7 in Supplementary Information.

Isotherm type	Isotherm equation	Fitted isotherm parameters			
		$\Delta I_{\text{normalized DPV, max}}$	$K, \mu\text{M}^{-1}$	n	R^2
Langmuir	$\Delta I_{\text{normalized DPV}} = \Delta I_{\text{normalized DPV, max}} \frac{K_L c_{\text{cilostazol}}}{1 + K_L c_{\text{cilostazol}}}$	0.59 (±0.048)	8.53 (±2.498) ^a	-	0.935
Freundlich	$\Delta I_{\text{normalized DPV}} = K_F c_{\text{cilostazol}}^{\frac{1}{n}}$	-	0.65 (±0.066) ^b	2.55 (±0.574) ^d	0.865
Langmuir-Freundlich	$\Delta I_{\text{normalized DPV}} = \Delta I_{\text{normalized DPV, max}} \frac{K_{LF} c_{\text{cilostazol}}^{\frac{1}{n}}}{1 + K_{LF} c_{\text{cilostazol}}^{\frac{1}{n}}}$	0.47 (±0.017)	12.72 (±1.152) ^c	2.09 (±0.431) ^e	0.971

$\Delta I_{\text{normalized DPV}}$ – normalized DPV peak current

$\Delta I_{\text{normalized DPV, max}}$ – maximum value of normalized DPV peak current

^a K_L – Langmuir constant

^b K_F – Freundlich constant

^c K_{LF} – Langmuir-Freundlich constant

^d Sorption intensity

^e Homogeneity factor

Table S2b. Parameters of isotherms fitted to the normalized DPV peak current dependence on the CIL concentration at the NIP film-coated electrode depicted in Figure S7 in Supplementary Information.

Isotherm type	Isotherm equation	Fitted isotherm parameters			
		$\Delta I_{\text{normalized DPV, max}}$	$K, \mu\text{M}^{-1}$	n	R^2
Langmuir	$\Delta I_{\text{normalized DPV}} = \Delta I_{\text{normalized DPV, max}} \frac{K_L}{1 + K_L C_{\text{cilostazol}}}$	0.93 (±1.181)	0.27 (±0.411) ^a	-	0.794
Freundlich	$\Delta I_{\text{normalized DPV}} = K_F C_{\text{cilostazol}}^{\frac{1}{n}}$	-	0.19 (±0.013) ^b	1.25 (±0.177) ^d	0.876
Langmuir-Freundlich	$\Delta I_{\text{normalized DPV}} = \Delta I_{\text{normalized DPV, max}} \frac{(K_{LF})^n}{1 + (K_{LF})^n C_{\text{cilostazol}}^n}$	0.99	0.17	0.77	0.834

$\Delta I_{\text{normalized DPV}}$ – normalized DPV peak current

$\Delta I_{\text{normalized DPV, max}}$ – maximum value of normalized DPV peak current

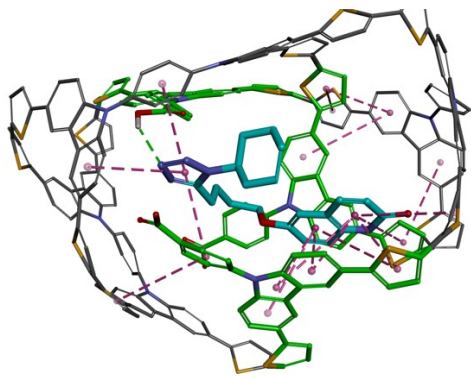
^a K_L – Langmuir constant

^b K_F – Freundlich constant

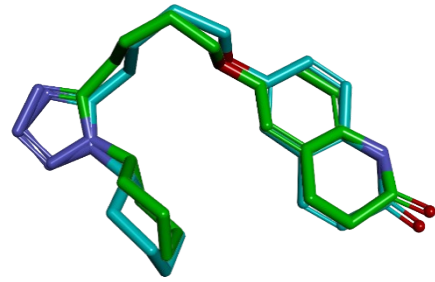
^c K_{LF} – Langmuir-Freundlich constant

^d Sorption intensity

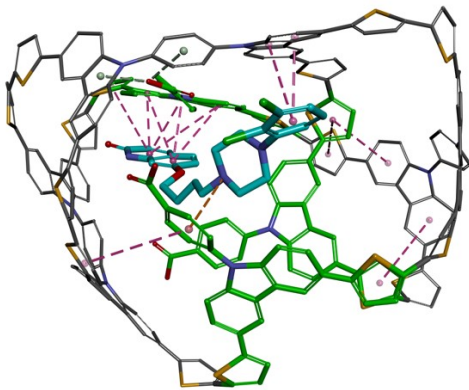
^e Homogeneity factor



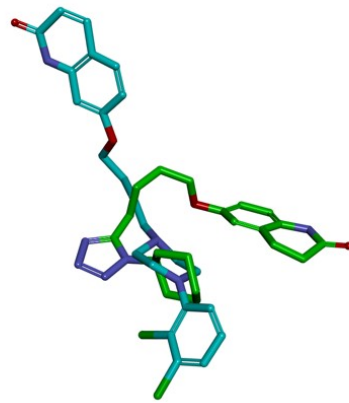
a



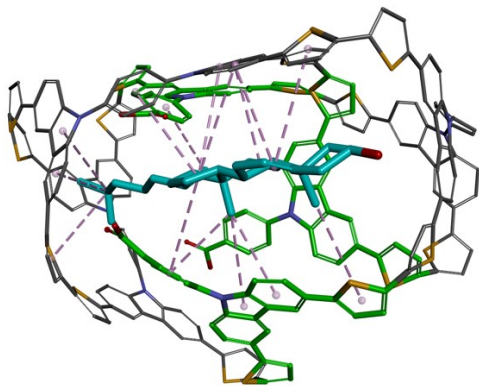
d



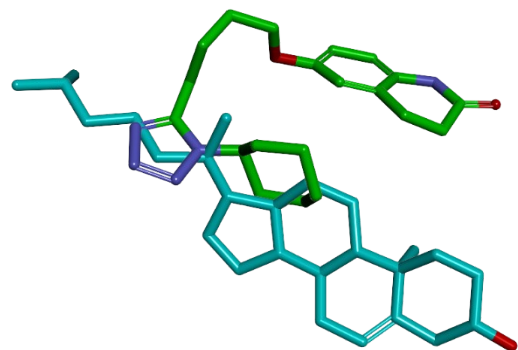
b



e



c



f

Figure S8. Skeleton models (left) of the imprinted cavity showing intermolecular interactions (dash lines) with (a) dhCIL, (b) dehydroaripiprazole, and (c) cholesterol. Conformational differences in the CIL-extracted MIP cavity (right) between CIL (green) and (d) dhCIL, (e) dehydroaripiprazole, and (f) cholesterol interferences (turquoise).

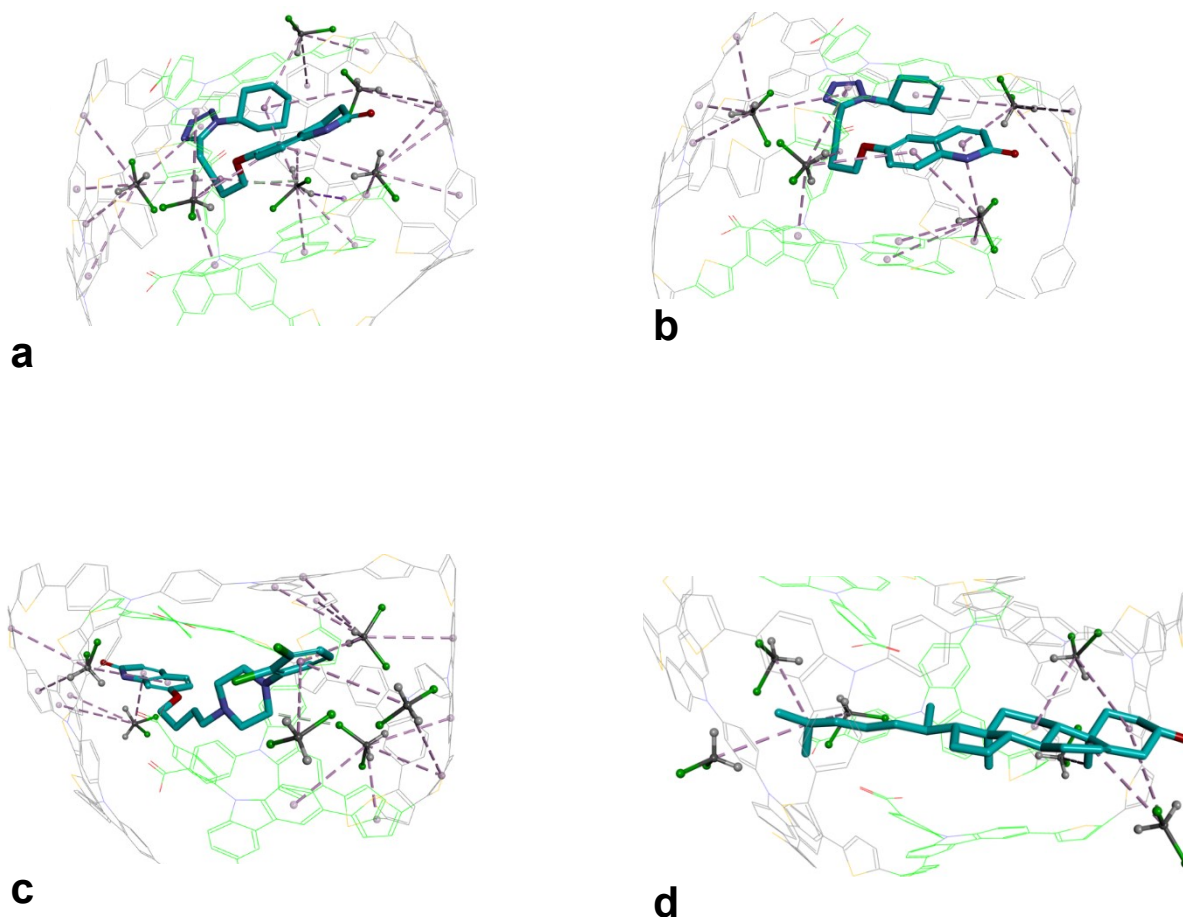


Figure S9. Skeleton views of the CIL-extracted MIP cavity with solvent molecules sorbed (purple lines – π -alkyl type hydrophobic interactions) and the molecules of (a) cilostazol (CIL), (b) 3,4-dehydrocilostazol (dhCIL), (c) dehydroaripiprazole, and (d) cholesterol present.

S11. Solvent impact on intermolecular interactions

All imprinting components should be dissolved in the appropriate solvent, but the solvent should not compete with the monomers in the polymerization and with analytes in the sorption on the other. The analyte molecules exchange the space with the DCM molecules in the cavity, but four to six solvent molecules are still left in it. The DCM molecules enabled additional contacts between the analyte, FM1, and CLM molecules, acting as a bridge between these molecules. The DCM contributed to the π -alkyl type network forming intermolecular interactions (length of 5.04 to 5.42 Å). The CIL, dhCIL, and dehydroaripiprazole molecules attract more DCM molecules than

cholesterol and form bridges with the cavity wall. Cholesterol interacts with DCM (length of 4.03 to 4.92 Å). Therefore, the DCM presence in the cavity weakens the formation of bridges of cholesterol with the FM1 or CLM. In the cases examined, DCM increases the stability of the analytes in the cavity and influences MIP's binding selectivity and capacity. CIL forms one strong hydrogen bond by its tetrazole ring with the carboxyl of FM1 (length of 2.62 Å) and one non-classical hydrogen bond (π -donor) by its NH group with the thiophene ring of one FM1 molecule (length of 3.20 Å), which hold molecule CIL in the cavity. The π - π stacked type interactions are generated between the quinolinone moiety of CIL and the tricyclic structure of the carbazole moiety of FM1 (length of 4.05 to 5.81 Å). Moreover, hydrophobic π - π T-shaped and π - π stacked types of interactions are established between the tetrazole ring of CIL and the tricyclic structure of the carbazole or benzene ring of CLM or FM1, respectively (Figure 4c). Like CIL, the dhCIL also interacts with FM1 and CLM (Figure S8a in Supplementary Information). However, minor differences in orientations of CIL and dhCIL molecules result in weaker hydrophobic interactions of the tetrazole ring (length of 5.65 to 5.34 Å) and the quinolinone moiety (length of 4.65 to 5.99 Å) of dhCIL with the cavity. Furthermore, there is only one strong hydrogen bond between the tetrazole moiety of dhCIL and the carboxyl group of FM1 (length 2.29 Å), which holds molecule dhCIL in the cavity. Examining cholesterol sorption in MIP-CIL revealed that cholesterol could compete to some extent with CIL and dhCIL, but its interactions with the cavity are weaker because it is positioned partially outside the cavity. Cholesterol forms only the π -alkyl type interactions (length 4.16 to 5.42 Å) with no hydrogen bonds between the analyte and the polymer (Figure S8c and S8f in Supplementary Information). Dehydroaripiprazole affinity to the cavity was the lowest because of the elongated conformation it assumes in the cavity. It interacts via π - π stacking between the dichlorobenzene moiety (length of 3.97 to 4.60 Å), the quinoline moiety (length of 4.31 to 5.53 Å), and the tricyclic fragment of the carbazole moieties of FM1 or CLM. There is one electrostatic interaction (π -cation) between the nitrogen atom of the piperazine moiety of dehydroaripiprazole and the aromatic ring of FM1 (Figure S8b and S8e in Supplementary Information).

Table S3. Parameters of Langmuir-Freundlich isotherms, fitted to the normalized ferrocene DPV peak current dependence on the CIL, dhCIL, cholesterol, and dehydroaripiprazole concentration, for the CIL-extracted MIP film-coated electrode.

Compound	Fitted isotherm parameters			
	$\Delta I_{\text{normalized DPV,max}}$	$K_{\text{LF}}^{\text{a}}, \mu\text{M}^{-1}$	n^{b}	R^2
Cilostazol	0.47 (± 0.02)	12.72 (± 1.15)	2.09 (± 0.43)	0.97
3,4-Dehydrocilostazol	1.75 (± 0.25)	0.23 (± 0.19)	0.48 (± 0.19)	0.99
Cholesterol	0.57 (± 0.04)	7.29 (± 0.92)	0.47 (± 0.02)	0.97
Dehydroaripiprazole	0.19	0.0001	0.0004	No fit

^a K_{LF} – Langmuir-Freundlich constant

^b n – homogeneity factor

Table S4. Comparison of analytical parameters of the presently devised chemosensor with some chemosensors and methods for cilostazol (CIL) determination reported in the literature.

Chemosensor composition or determination principle	CIL linear dynamic concentration range	Limit of detection (LOD)	Detection method	Ref.
MIP film	50 - 923.6 nM	15 nM	Electrochemical (DPV)	This work
nanoMIPs@polytyramine	134 nM - 2.58 μ M	93.5 nM (DPV) 86.5 nM (EIS)	Electrochemical (DPV, EIS)	10
Bismuth/multi-walled carbon nanotubes	2.1 - 33.8 μ M	2.057 μ M	Electrochemical (CV)	11
Enhancement of the green emission of Tb ³⁺	1 nM - 1 μ M	0.75 nM	Optical (luminescence)	12
Carbon paste electrode	0.4 - 6.4 μ M	0.4 μ M	Electrochemical (DPV)	13

References

(1) Gajda, M.; Rybakiewicz, R.; Cieplak, M.; Żółek, T.; Maciejewska, D.; Gilant, E.; Rudzki, P. J.; Grab, K.; Kutner, A.; Borowicz, P.; Kutner, W.; Noworyta, K. R. Low-Oxidation-Potential Thiophene-Carbazole Monomers for Electro-Oxidative Molecular Imprinting: Selective Chemosensing of Aripiprazole. *Biosens. Bioelectron.* **2020**, *169*, 112589.

(2) Dassault Systèmes BIOVIA. Discovery Studio Modeling Environment., Release 2017. San Diego: Dassault Systèmes, 2016.

(3) Wishart, D. S.; Feunang, Y. D.; Guo, A. C.; Lo, E. J.; Marcu, A.; Grant, J. R.; Sajed, T.; Johnson, D.; Li, C.; Sayeeda, Z.; Assempour, N.; Iynkkaran, I.; Liu, Y.; Maciejewski, A.; Gale, N.; Wilson, A.; Chin, L.; Cummings, R.; Le, Di.; Pon, A.; Knox, C.; Wilson, M. DrugBank 5.0: A Major Update to the DrugBank Database for 2018. *Nucleic Acids Res.* **2018**, *46*, D1074–D1082.

(4) Frisch, M. J.; Trucks, G. W.; Schlegel, H. B.; Scuseria, G. E.; Robb, M. A.; Cheeseman, J. R.; Scalmani, G.; Barone, V.; Petersson, G. a.; Nakatsuji, H.; Li, X.; Caricato, M.; Marenich, A. V.; Bloino, J.; Janesko, B. G.; Gomperts, R.; Mennucci, B.; Hratchian, H. P.; Ortiz, J. V.; Izmaylov, A. F.; Sonnenberg, J. L.; Williams; Ding, F.; Lipparini, F.; Egidi, F.; Goings, J.; Peng, B.; Petrone, A.; Henderson, T.; Ranasinghe, D.; Zakrzewski, V. G.; Gao, J.; Rega, N.; Zheng, G.; Liang, W.; Hada, M.; Ehara, M.; Toyota, K.; Fukuda, R.; Hasegawa, J.; Ishida, M.; Nakajima, T.; Honda, Y.; Kitao, O.; Nakai, H.; Vreven, T.; Throssell, K.; Montgomery Jr., J. a.; Peralta, J. E.; Ogliaro, F.; Bearpark, M. J.; Heyd, J. J.; Brothers, E. N.; Kudin, K. N.; Staroverov, V. N.; Keith, T. a.; Kobayashi, R.; Normand, J.; Raghavachari, K.; Rendell, a. P.; Burant, J. C.; Iyengar, S. S.; Tomasi, J.; Cossi, M.; Millam, J. M.; Klene, M.; Adamo, C.; Cammi, R.; Ochterski, J. W.; Martin, R. L.; Morokuma, K.; Farkas, O.; Foresman, J. B.; Fox, D. J., Gaussian 16, Inc. Wallingford CT,

USA, 2016.

(5) Breneman, C.; Wiberg, K. Determining Atom-Centered Monopoles from Molecular Electrostatic Potentials. The Need for High Sampling Density in Formamide Conformational Analysis. *J. Comput. Chem.* **1990**, *11*, 361–373.

(6) Brooks, B. R.; Brucoleri, R. E.; Olafson, B. D.; States, D. J.; Swaminathan, S.; Karplus, M. CHARMM: A Program for Macromolecular Energy, Minimization, and Dynamics Calculations. *J. Comput. Chem.* **1983**, *4*, 187–217.

(7) Cheatham, T. E. I. I.; Miller, J. L.; Fox, T.; Darden, T. A.; Kollman, P. A. Molecular Dynamics Simulations on Solvated Biomolecular Systems: The Particle Mesh Ewald Method Leads to Stable Trajectories of DNA, RNA, and Proteins. *J. Am. Chem. Soc.* **1995**, *117*, 4193–4194.

(8) Essmann, U.; Perera, L.; Berkowitz, M. L.; Darden, T.; Lee, H.; Pedersen, L. G. A Smooth Particle Mesh Ewald Method. *J. Chem. Phys.* **1995**, *103*, 8577–8593.

(9) Martinez, L.; Andrade, R.; Birgin, E. G.; Martinez, J. M. Packmol: A Package for Building Initial Configurations for Molecular Dynamics Simulations. *J. Comput. Chem.* **2009**, *30*, 2157–2164.

(10) Jyoti; Gonzato, C.; Żołek, T.; Maciejewska, D.; Kutner, A.; Merlier, F.; Haupt, K.; Sharma, P. S.; Noworyta, K. R.; Kutner, W. Molecularly Imprinted Polymer Nanoparticles-Based Electrochemical Chemosensors for Selective Determination of Cilostazol and Its Pharmacologically Active Primary Metabolite in Human Plasma. *Biosens. Bioelectron.* **2021**, *193*, 113542.

(11) Jain, R.; Sharma, R. Novel Bismuth / Multi-Walled Carbon Nanotubes-Based Electrochemical Sensor for the Determination of Neuroprotective Drug Cilostazol. *J. Appl. Electrochem.* **2012**, *42*, 341–348.

(12) Attia, M. S.; Mahmoud, W. H.; Youssef, A. O.; Mostafa, M. S. Cilostazol Determination by the Enhancement of the Green Emission of Tb³⁺ Optical Sensor. *J. Fluoresc.* **2011**, *21*, 2229–2235.

(13) Wassel, A.; Amin, A.; Ahmed, I.; Dessouki, H.; Hendawy, H. Electrochemical Behavior and Determination of Cilostazol in Pure, Urine and in Pharmaceutical Formulations. *Anal. Bioanal. Electrochem.* **2012**, *4*, 197–211.